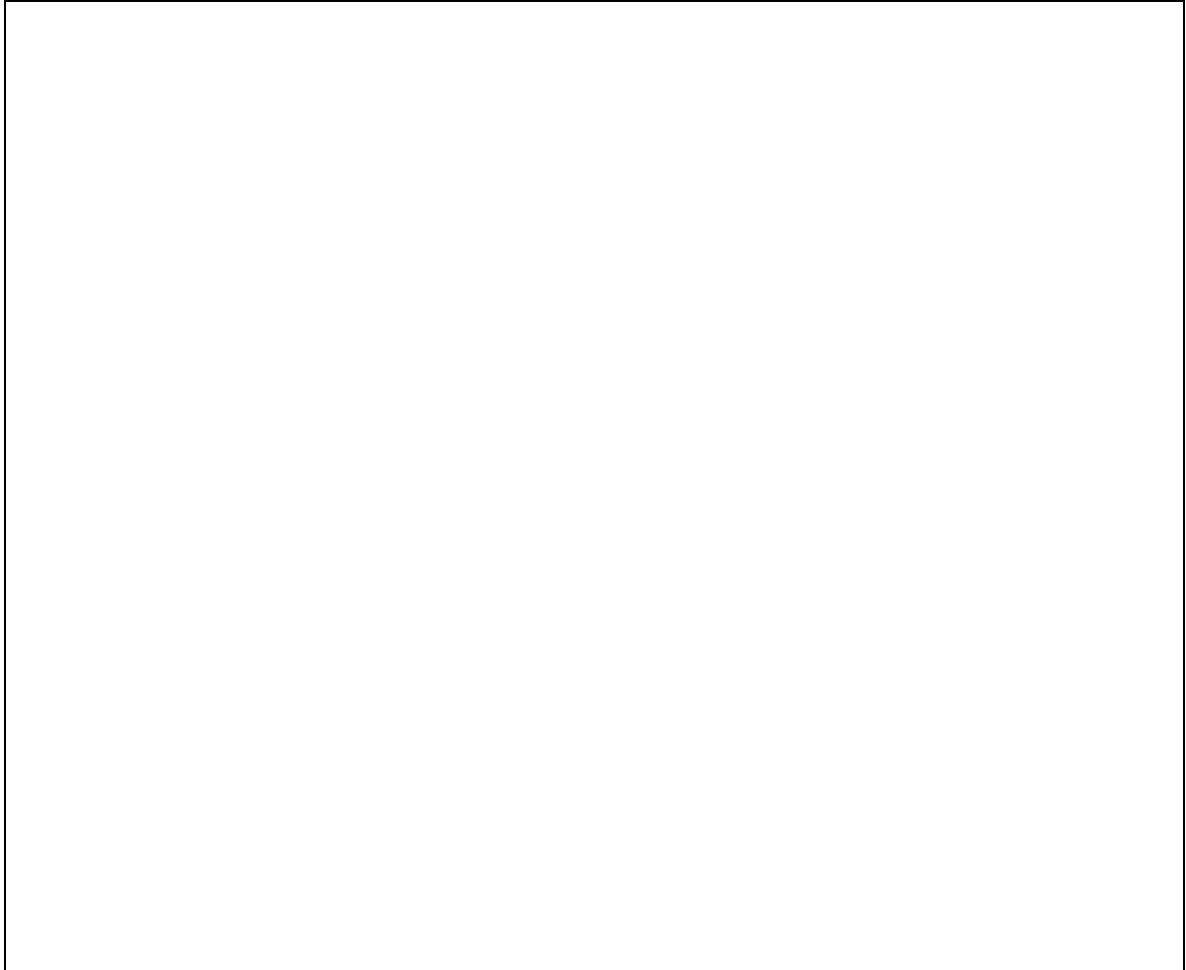


Assessment of Surface Subsidence Associated with Caving
Resolution Copper Mine Plan of Operations



ITASCA
Consulting Group, Inc.

*Assessment of Surface Subsidence Associated with Caving
Resolution Copper Mine Plan of Operations*



July 17, 2017
2-5605-01:17R25



Prepared For:
Resolution Copper Mining LLC

Prepared By:
Tryana Garza-Cruz,
Itasca Consulting Group, Inc.
Matthew Pierce,
Pierce Engineering

111 Third Ave South, Suite 450
Minneapolis, MN 55401
phone: 1 612 371-4711 fax: 1 612 371-4711
email: icg@itascacg.com
web: www.itascacg.com

Executive Summary

This report summarizes the results of geomechanical studies of cave growth and subsidence potential performed by Itasca Consulting Group, Inc. (Itasca) for Resolution Copper Mining, LLC (Resolution Copper).

The subsidence impact model was run to support the mine plan of operations, which was submitted to the United States Forest Service (USFS) in November 2013 to initiate the comprehensive environmental review under the National Environmental Policy Act (NEPA) with the completion of an Environmental Impact Statement (EIS). The subsidence model was re-run to incorporate new geological data from drilling collected since 2011, including faults and geological spatial definition. This update is the basis for the present study.

The main purpose of this study is to evaluate the potential ground collapse and surface deformations associated with caving at Resolution Copper for the EIS based on a production schedule of approximately 135,000 short tons per day (120,000 metric tonnes per day).

The faults were qualitatively ranked as strong, medium, or weak based on their character. As a conservative reasonable approach, the strong and medium faults were assigned 75% and 50% of the local rock mass global strength (σ_{cm}), respectively, while the weak faults were assumed to have a very conservative zero cohesion, zero tensile strength, and 35° friction angle.

The caving simulations conducted suggest good caveability, with the cave reaching the ground surface at approximately year 6. This is due to the high ratio of in-situ horizontal stress to rock mass strength ratio. The average bulking factor of rock within the mobilized zone limits is predicted to increase gradually from 11.4% at year 5 to approximately 15.8% at year 41. At the end of mine life, the cave angles are expected to be of the order of 70–78°, with a maximum crater depth of approximately 340 m (1115 ft). At the end of mine life, the cave aims to achieve a more circular shape in plan, as this is the most stable (due to the confining effects of hoop stress).

The model predicts that caving would not affect the serviceability of highway US-60, and no damage is predicted to Devil's Canyon nor the Apache Leap.

Table of Contents

Executive Summary i

Table of Contents ii

1.0 Introduction 1

2.0 Proposed Mine Design 1

3.0 Numerical Model Geometry and Description 2

4.0 Geotechnical Properties..... 4

 4.1 Geology 4

 4.2 Structural Geology 5

 4.3 Rock Mass Strength 10

 4.3.1 Peak Rock Mass Strength Parameters 10

 4.3.2 Residual Rock Mass Strength 11

 4.4 In-situ Stress 12

5.0 Numerical Approach to Analysis of Caving 13

6.0 Caving and Subsidence Predictions 14

 6.1 Caveability and Subsidence Results..... 14

 6.1.1 Bulking Factors, Caving Rate, and Breakthrough Timing 15

 6.1.2 Subsidence Impact Analysis — Results 16

7.0 Conclusions 21

8.0 References 22

Appendix 1 23

 1.0 Numerical Approach to Analysis of Caving 23

 1.1 FLAC3D 23

 1.2 Conceptual Model of Caving 23

 1.3 Background 25

 1.4 The Cave-Hoek Constitutive Model 28

 1.5 Draw Simulation 29

 1.6 Bulked Rock Properties 30

1.6.1	Maximum Porosity.....	30
1.6.2	Hoek-Brown Residual Properties.....	30
2.0	Cave-Hoek Constitutive Model.....	30
2.1	Input Properties	30
2.2	Bulking.....	32
2.3	Density Adjustment.....	33
2.4	Tension Weakening.....	33
2.5	Cohesion Weakening.....	34
2.6	Modulus Softening	35
2.7	Dilation Shutoff.....	39

1.0 INTRODUCTION

The use of caving as a mass mining method is anticipated to result in surface subsidence and settling of ground. Caving-induced subsidence may put mine infrastructure at risk. Therefore, the ability to predict surface subsidence has become increasingly important for operational risk and environmental impact assessment. The term subsidence used in this report encompasses a wide range of surface effects associated with caving and not just the vertical displacement of the surface.

Caving-induced surface subsidence is typically characterized by three key zones: the crater (often derived from the mobilized zone), the fractured zone, and the zone of continuous subsidence. The limits and shapes of these zones are mainly controlled by the geological spatial distribution and its associated rock mass strength, in-situ stress, presence of major structures, preferred joint orientations, topography, and footprint depth and shape.

Empirical models are widely used in the early stages of mine design to describe the possible ground response as a consequence of mining based on observations and experience of actual mining subsidence. As noted by Flores & Karzulovic (2002), only numerical models allow the full extent of the influence zone to be predicted.

This report summarizes the results of geomechanical studies of cave growth and subsidence potential performed by Itasca Consulting Group, Inc. (Itasca) for Resolution Copper.

The main purpose of this study is to assess the potential ground collapse and surface deformations associated with caving at Resolution Copper for operational risk and environmental impact assessment based on a production schedule of approximately 135,000 tons per day (120,000 short tons per day). The model uses the latest available geological data, including updated faults and geological spatial definition and properties.

2.0 PROPOSED MINE DESIGN

Given the depth and size of the deposit, Resolution proposes to mine the orebody via a subset of block caving called panel caving. The extraction level would be located at an elevation of -2540 ft below MSL (a depth of approximately 2050 m below ground surface). The orebody is blind (does not daylight), with maximum column heights of the order of 550 m. The design proposed for analysis by Resolution is shown in Figure 1 along with the panel sequencing.

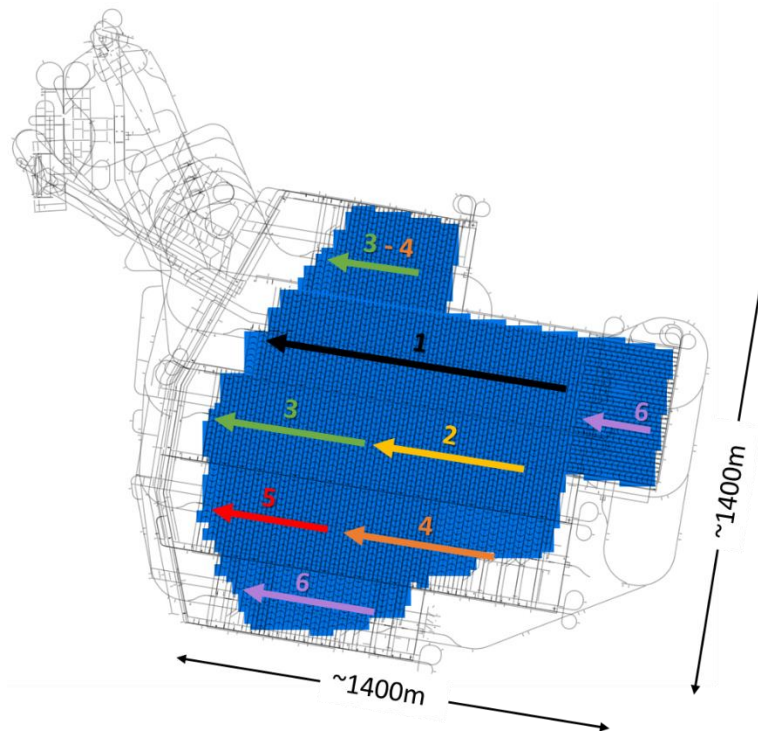


Figure 1 Proposed layout.

The spatial location of all draw points along with their associated production per period (quarterly) was provided by Resolution. The production profile is characterized by:

- a peak production of approximately 47.5 million tonnes/year;
- a ramp-up period of approximately 8 years;
- a ramp-down period of 10 years; and
- a total production at the end of mine life of approximately 1,400 million tonnes.

This production schedule was given as an input to the model.

3.0 NUMERICAL MODEL GEOMETRY AND DESCRIPTION

A large-scale industry standard *FLAC3D* (Itasca, 2017) model was constructed to simulate the regional extents of the Resolution mine. The model dimensions are approximately 15.2 km x 12.64 km x 3 km and consist of about 940,000 zones. The zones surrounding the extraction level, as well as near the ground surface where the subsidence is expected to occur, were densified to an edge length of approximately 20 m. The edge length is gradationally increased away from the area of interest to 40, 80, and 160 m closer to the model limits. The mesh was also densified in the vicinity of faults.

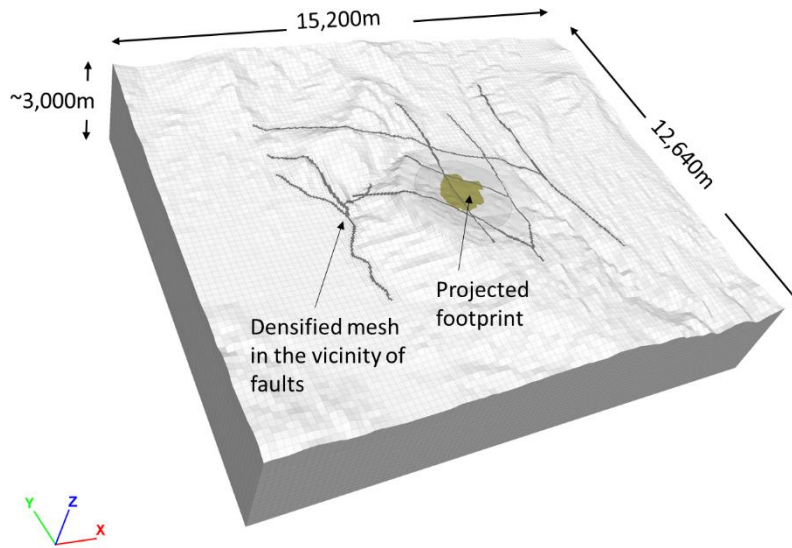


Figure 2 Model used for analysis.

A north-south and an east-west cross-section were established along the model to aid in visualization and analyze cave growth, as shown in Figure 3. For consistency, all cross-sectional views showed in this report correspond to one of these two sections.

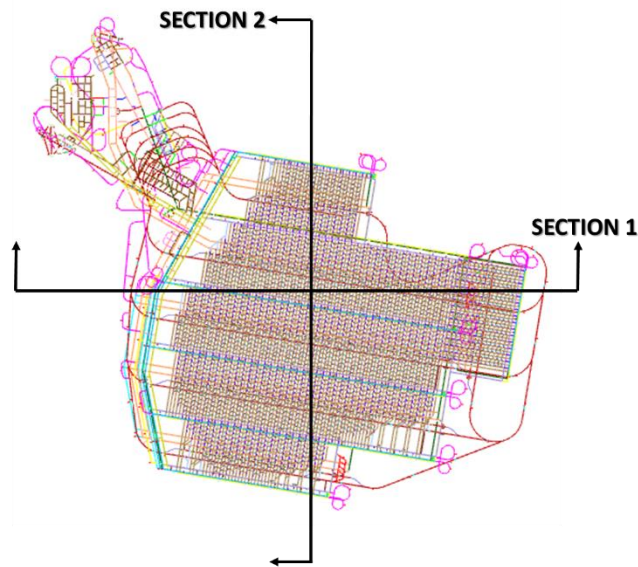


Figure 3 Location of the cross-sections used to analyze cave growth.

4.0 GEOTECHNICAL PROPERTIES

4.1 Geology

The geological interpretation used in the numerical model was provided by Resolution Copper as a series of DXF wireframes with associated hierarchy, as some of these solids overlapped. These DXFs were directly used in the *FLAC3D* model to introduce the spatial distribution of the different geological units, as shown in Figure 4 and Figure 5 on the east-west cross-sectional plane (looking north, see Figure 3) and on the north-south section (looking west), respectively. The production level is at an elevation of -2540 ft below MSL, approximately 2050 m below surface on average.

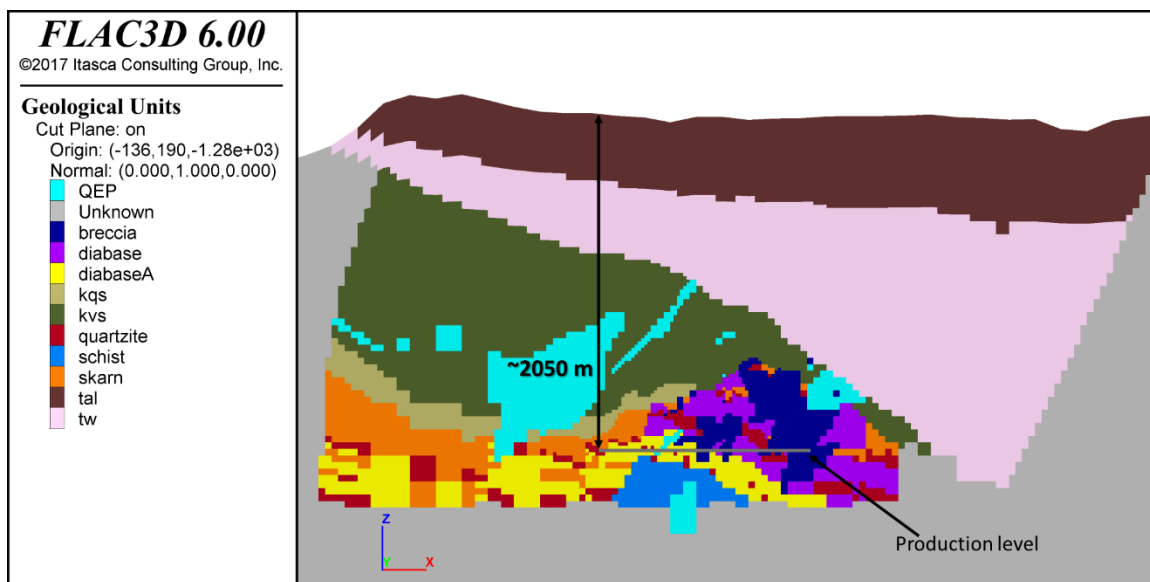


Figure 4 *Spatial distribution of lithology on an east-west cross-section looking north.*

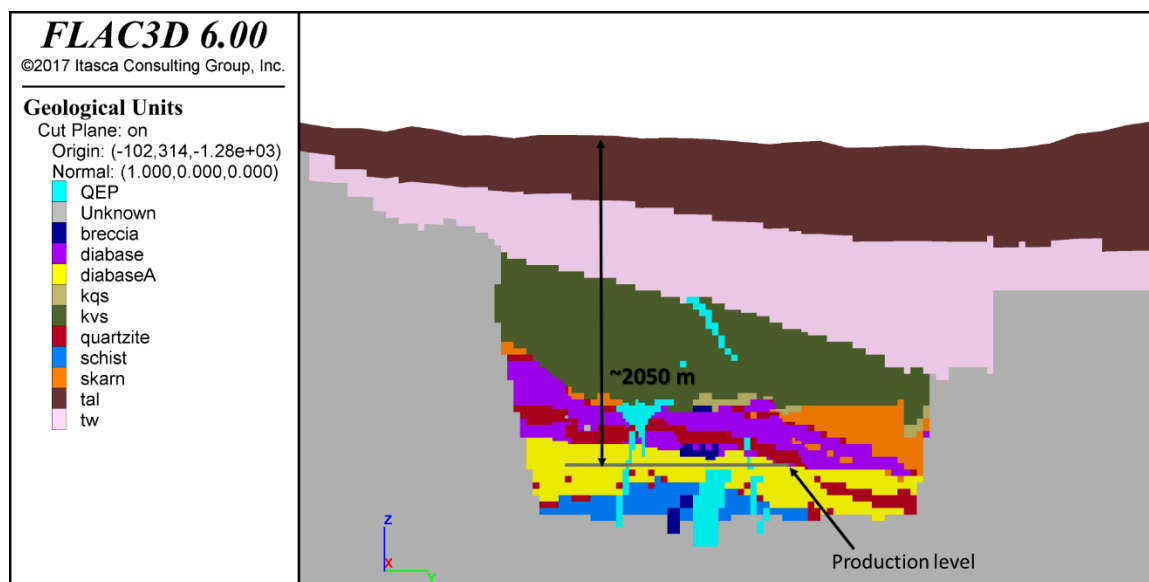


Figure 5 Spatial distribution of lithology on north-south cross-section looking west.

4.2 Structural Geology

The structural geology was provided by Resolution Copper personnel in the form of 3D triangulated surfaces along with their associated description. The faults were implicitly incorporated into the model as regions of weaker and softer material. Figure 6 shows the spatial location of the faults with respect to the projection of the footprint. The faults were qualitatively ranked as strong, medium, or weak based on their character. In general, faults described as either slickensided shears, heavily damaged, brecciated, and/or with gouge were classified as weak. Faults described as either mixed open and/or annealed shears, with local gouge and/or with local intense damage, were classified as medium, while those described as strongly annealed were classified as strong. Table 1 lists the qualitative ranking of the faults used in the analysis presented in this report. The spatial distribution of lithology units along with modeled faults intersected by an east-west and north-south cross-section are shown in Figure 7 and Figure 8, respectively.

Table 1 Qualitative Ranking of the Faults Used in the FLAC3D Model

Strong (75% σ_{cm})	Medium (50% σ_{cm})	Weak (residual prop)
Manske	Andesite	326 Pump Station
Monarch	Camp	Anxiety
MP-1	Hammer N	Concentrator
MP-2	Hammer S	Conley Spring
MP-3	Hammer SW	Devils Canyon
South Boundary	Intergraben	Gant E
	North Boundary A	Gant W
	North Boundary B	Main
	North Boundary C	North Boundary
	Paul	Rancho Rio
	Paul S	West Boundary
	Peterson	
	Superior	
	Superior A	

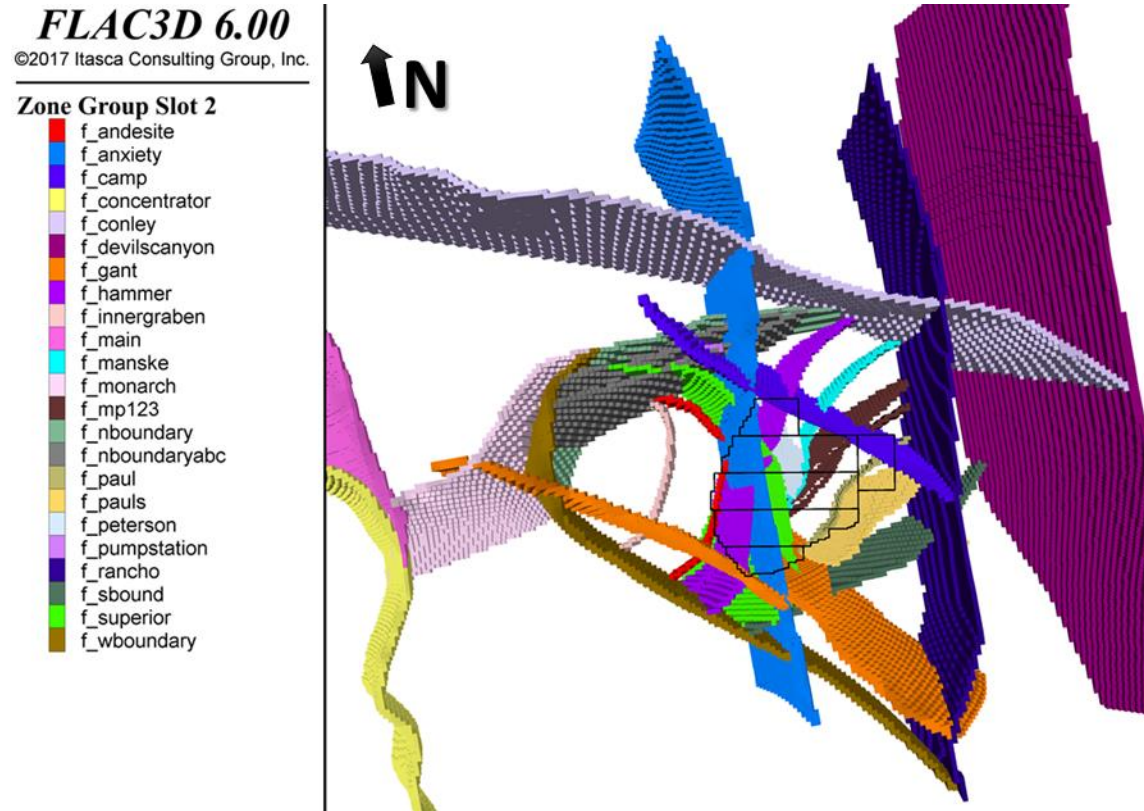


Figure 6 *FLAC3D implicit representation of the faults in the region of the Resolution Mine footprint.*

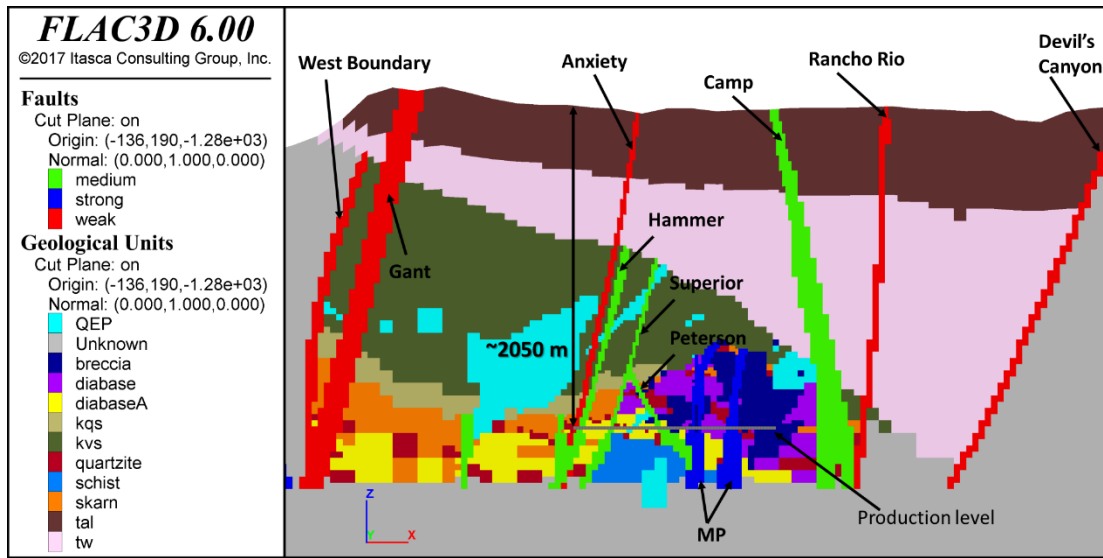


Figure 7 Spatial distribution of lithology on an east-west cross-section looking north. The intersected faults are colored based on their qualitative ranking (medium, strong, and weak).

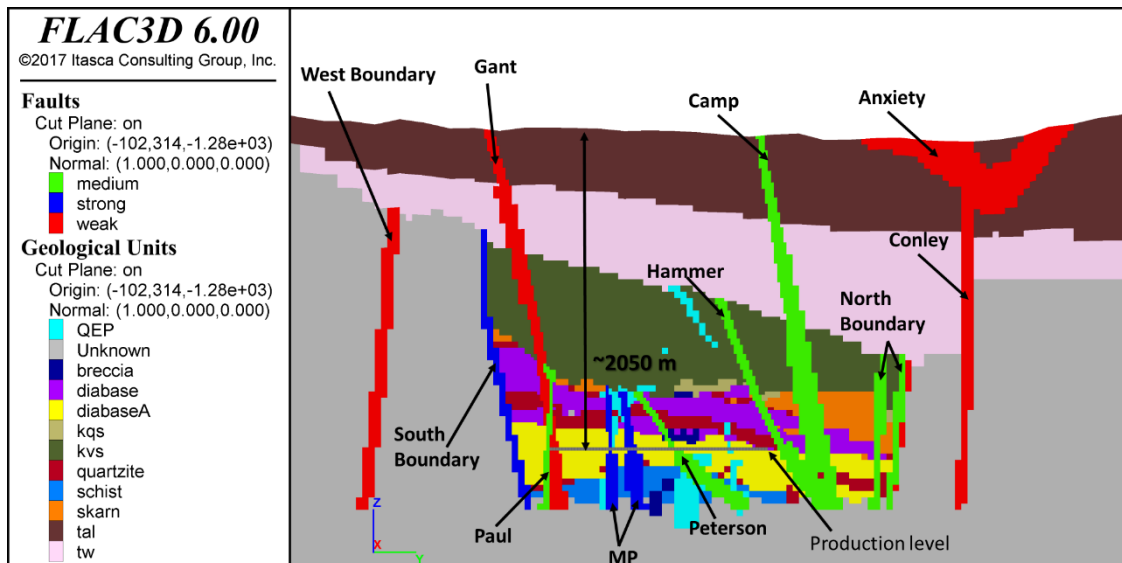


Figure 8 Spatial distribution of lithology on north-south cross-section looking west. The intersected faults are colored based on their qualitative ranking (medium, strong, and weak).

The strong and medium faults were assigned 75% and 50% of the local rock mass global strength (σ_{cm}), respectively, while the weak faults were assumed to have zero cohesion, zero tensile strength, and 35° friction angle (Table 2). This is a conservative approach because some of the

strong faults that display annealing properties display stronger in-situ strength than the surrounding rock. σ_{cm} is the unconfined compressive strength defined by a Mohr-Coulomb fit to the Hoek-Brown curve over a range of confinement from 0 to 25% of the laboratory intact uniaxial compressive strength (UCS). In order to simplify the process of assigning the desired percentage of the local rock-mass global-strength (a function of both the geological strength index (GSI) and UCS), a relationship between the effect of equally varying both the GSI and UCS to obtain the resulting global strength was generated, as shown in Figure 10. The qualitative ranking and strength characterization was discussed and approved by Resolution personnel (personal communication, Jacques Tshisens). The relative classification of faults persistent to ground surface is shown in Figure 9.

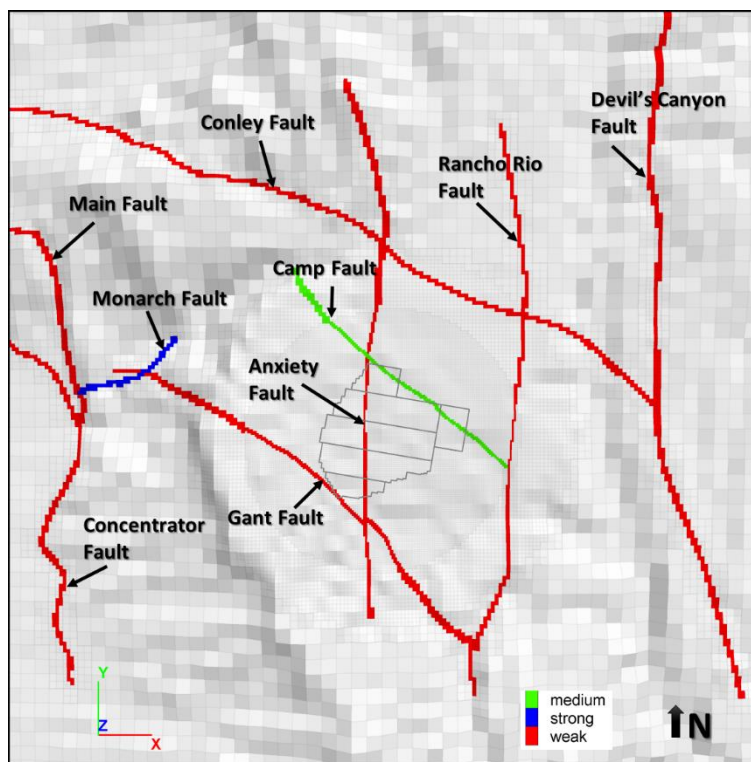


Figure 9 Faults persistent to surface and their relative classification.

Table 2 Fault Properties for the Study

	Properties
Strong Faults	$0.75 \sigma_{cm}$
Medium Faults	$0.5 \sigma_{cm}$
Weak Faults	Cohesion = 0 Tensile strength = 0 Friction = 35°

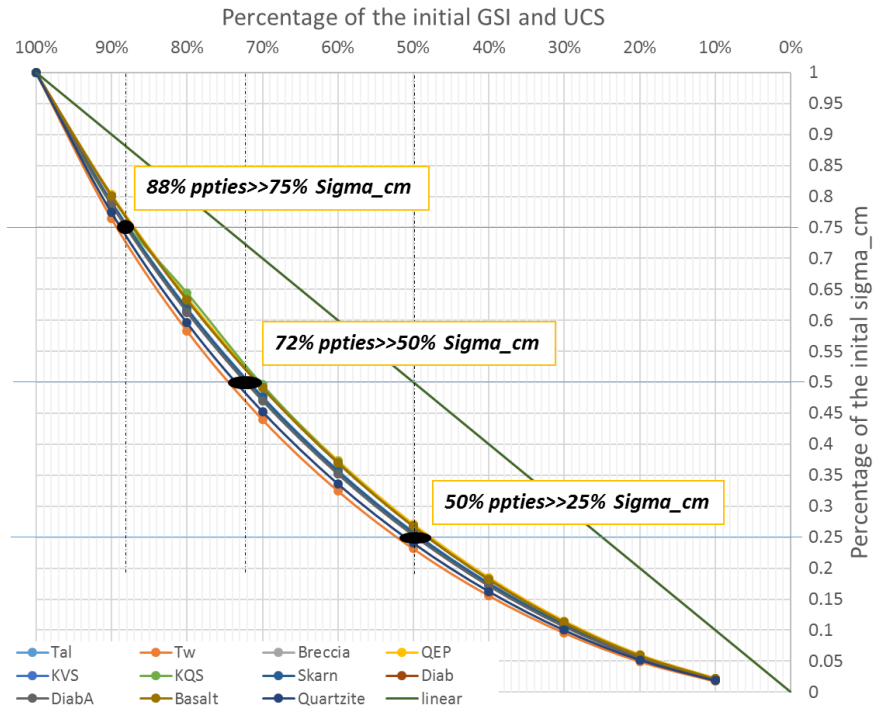


Figure 10 Relationship between initial GSI and UCS and resulting global strength (σ_{cm}).

4.3 Rock Mass Strength

4.3.1 Peak Rock Mass Strength Parameters

The rock mass properties for the different geological units were provided by Resolution Copper.

GSI was deemed by Resolution staff to be applicable to the study of large-scale caving, considering both the scale of the problem and the guidelines provided by Rio Tinto. Given the values of E_d (Young’s modulus of the defected rock) provided by Resolution, the rock mass modulus can be calculated directly from:

$$E_{rm} = E_d \left(0.02 + \frac{1 - \frac{D}{2}}{1 + e^{\left(\frac{60 + 15D - GSI}{11}\right)}} \right) \quad \text{Eq 1}$$

Where the disturbance factor D is assumed to be 0.

The m parameter for the rock mass, m_{rm} , is assessed by downgrading the m parameter for the defected rock, m_d , based on:

$$m_{rm} = m_d e^{\left(\frac{GSI-100}{28}\right)} \quad \text{Eq 2}$$

Where the parameters s and a are based on the GSI as follows:

$$s = e^{\left(\frac{GSI-100}{9}\right)} \quad \text{Eq 3}$$

$$a = \frac{1}{2} + \frac{1}{6} \left(e^{-GSI/15} - e^{-20/3} \right) \quad \text{Eq 4}$$

Table 3 lists the rock mass parameters of the geological units present in the model.

Table 3 *Provided Data and Estimated Hoek-Brown Parameters used in the FLAC3D Model by Geologic Unit*

	Data				3D Model Parameters					
	Unit	GSI	σ_d (MPa)	md	Ed (GPa)	Density	Erm (Gpa)	v	Peak Strength	
mrm									s	a
Diabase, Basalt	54	54	12	27	2600	10.4	0.24	2.3	0.006	0.5
Diabase with anhydrite	62	106	15	40	2600	22.6	0.23	3.9	0.0147	0.5
Breccia, QEP	54	55	15	31	2600	12	0.24	2.9	0.006	0.5
Quartzite	69	103	21	39	2600	27.8	0.22	6.9	0.0319	0.5
Tal (Apache Leap Tuff)	64	66	30	30	2600	18	0.22	8.2	0.0175	0.5
Tw (Whitetail)	73	23	22	10	2600	7.8	0.21	8.3	0.0476	0.5
KVS, KQS	66	46	30	30	2600	19.3	0.22	8.8	0.0217	0.5
Skarn	63	59	22	40	2600	23.1	0.23	5.8	0.0155	0.5

4.3.2 Residual Rock Mass Strength

Because the focus of this analysis is to evaluate the potential surface subsidence as a result of caving, the most relevant behavior is that of the rock mass in the periphery of the cave (fractured zone), which is typically yielded but not mobilized (therefore not bulked significantly), as well as the elastic deformations that encompass the continuous subsidence zone. Therefore, it makes

sense to use the residual properties of a rock mass that has yielded but not experienced significant bulking, that is, a friction angle of the order of 50°.

4.4 In-situ Stress

The stress regime used for the analysis presented here was provided by Resolution and is based upon hydrofracturing tests done on site.

- The major principal stress, σ_1 , is the vertical stress and is equal to the overburden.
- The intermediate principal stress (or maximum horizontal stress) σ_2 is oriented in a north-south direction and has a magnitude of 80% of σ_1 .
- The minimum principal stress (and minimum horizontal stress) σ_3 is oriented in the east-west direction and has a magnitude of 50% of σ_1 .

The magnitude of the stress field used in the analysis are listed in Table 4 and compared in graphical form in Figure 11.

Table 4 In-Situ Stress Field Used

Principal Stress	Magnitude
σ_v	25.5*z [km]
σ_h	20.4*z [km]
σ_H	12.75*z [km]

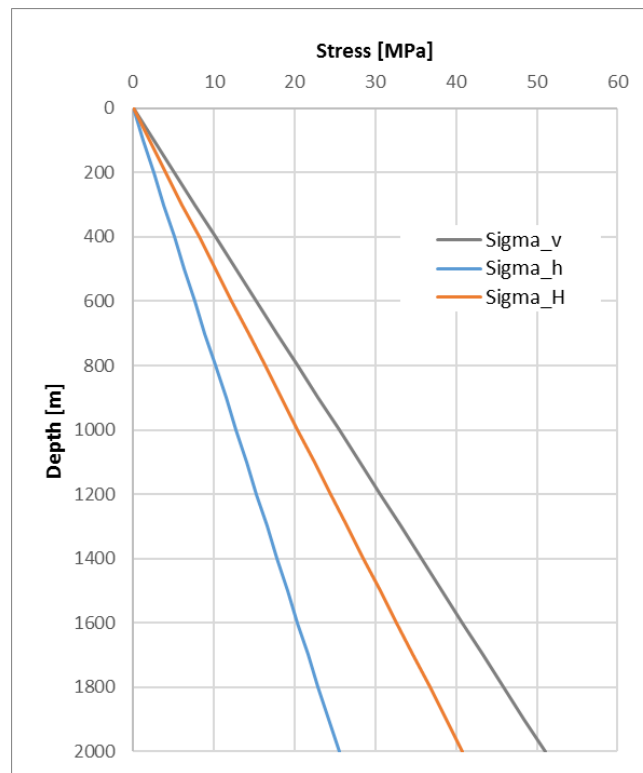


Figure 11 *In-situ stress regime used in the analysis.*

5.0 NUMERICAL APPROACH TO ANALYSIS OF CAVING

A detailed description of the caving algorithm that applies to all types of caving operations (block cave, panel cave, sublevel cave) is presented in Appendix 1. This algorithm has been developed by Itasca and used to simulate cave growth successfully at many other mines around the world. Additionally, a detailed description of the Cave-Hoek constitutive model that was used for this study is also presented in Appendix 1.

6.0 CAVING AND SUBSIDENCE PREDICTIONS

6.1 Caveability and Subsidence Results

The main purpose of this study is to identify the potential surface subsidence for the proposed Resolution mining operations based on the production described in Section 2.0. This section outlines the results of simulations and gives predictions of cave shape, bulking factors, caving rate, surface breakthrough timing and subsidence limits.

The conditions examined in this study correspond to the following:

- rock mass properties listed in Table 3;
- in-situ stress ($\sigma_H=0.8\times\sigma_v$ oriented in the north-south direction and $\sigma_H=0.8\times\sigma_v$ in the east-west direction, see Table 4); and
- faults with strength outlined in Table 2.

Throughout this document, the mobilized zone is defined as a region with vertical displacement exceeding 2 m and is used to delineate the crater limits. The fractured zone is defined as a region with the total measure of strain exceeding 0.5% and is used to determine the limits of visible fracturing that would be expected from orebody extraction. The continuous subsidence limit is the area outside the fractured zone and is characterized by small continuous subsidence deformations that can only be detected using high resolution monitoring instrumentation. In this report, the continuous subsidence limit is calculated by the combination of horizontal strain and angular distortion that exceed the limit shown in purple in Figure 12. This limit is subjective to the standards followed by each mine as their tolerance to subsidence differ.

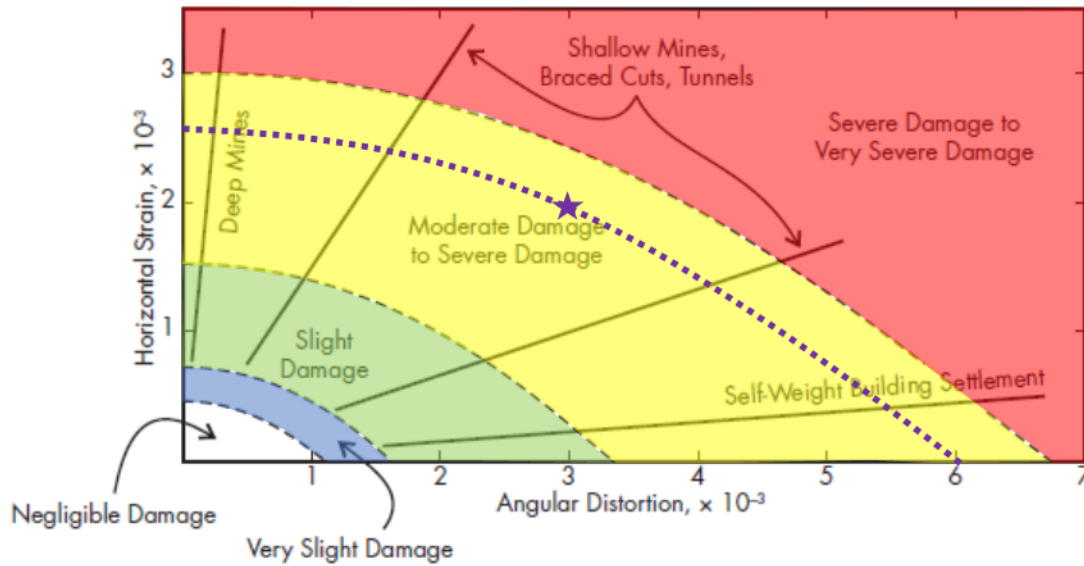


Figure 12 Building damage in terms of angular distortion and horizontal strain. The star and dotted purple line demarcate the continuous subsidence limit used in this analysis. Modified after Harrison (2011).

6.1.1 Bulking Factors, Caving Rate, and Breakthrough Timing

Caving rate is defined by the height of the yielded/fractured zone limit relative to the height of draw (meters of solid rock pulled). The caving rate is affected by several factors, including the bulking potential of the rock mass, the relative production rates (e.g., uniform draw results in less bulking and a faster caving rate), the presence of faults, rock mass brittleness, and rock mass strength.

The caving rate at Resolution is predicted to lie somewhere between 5.8 and 16.8 (see Figure 13). At these rates, the fracture limit reaches the ground surface around Year 6. This caving rate range is consistent with other reported caving rates around the world as shown in Figure 14. The average bulking factor of rock within the mobilized zone limits is predicted to increase gradually from 11.4% at year 5 to approximately 15.8% at year 41. This corresponds well with the cave bulking factors commonly reported for caving mines.

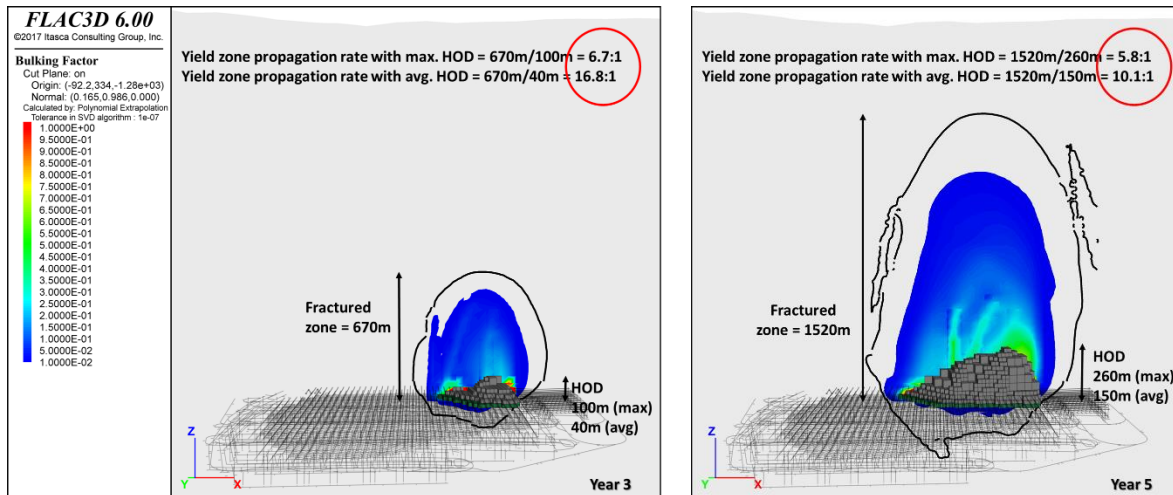


Figure 13 Determination of caving rate.

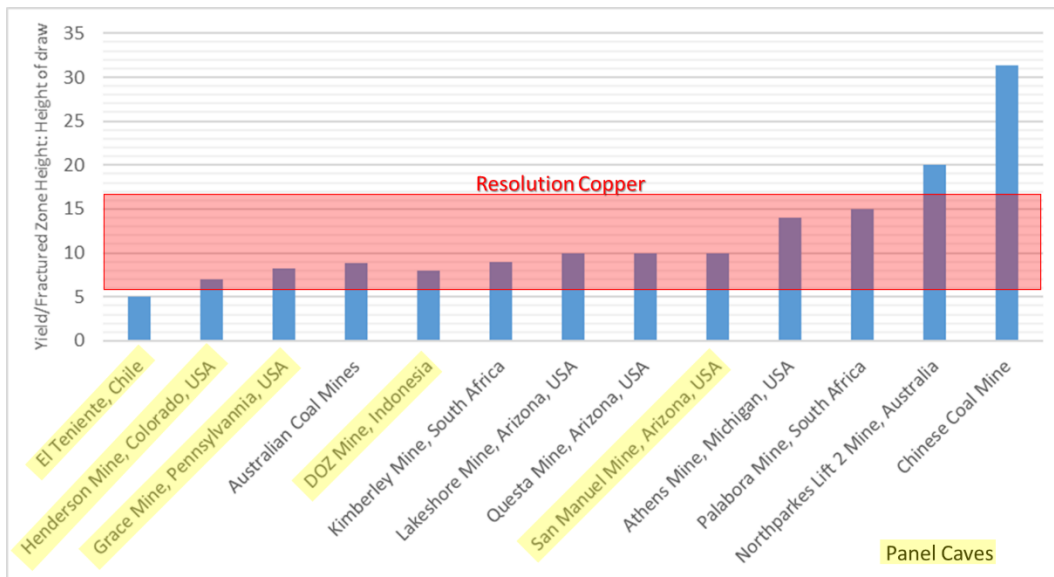


Figure 14 Comparison of caving rate predicted for Resolution to caving rate operations around the world (after Sainsbury and Sainsbury, 2010).

6.1.2 Subsidence Impact Analysis — Results

The simulation conducted for Resolution suggests good caveability, with continuous upward growth that breaks into the surface at year 6. The impact of major faults on cave growth and subsidence was examined by implicitly representing them as weakened zones coincident with the location of faults with properties listed in Table 2.

In the first years of production, the Camp, Superior, and Hammer faults pull out the fractured zone at depth. By year 8, the Anxiety fault has served as a channel for the cave to advance

rapidly upwards, while also serving as a release plane, compartmentalizing the cave. By year 15, the Camp and Gant faults have pulled the mobilized zone further out from the extraction level footprint, effectively widening the cave footprint. As the cave is further drawn down, additional confinement is lost near the surface, encouraging yielding farther than at depth. As production approaches the life of mine, the south boundary fault pulls the cave even further out at depth. Although the south boundary fault does not extend to surface, its impact on the cave size and shape at depth results in further expansion of the cave to the south at surface. This is an example of how the presence of faults at depth can affect the surface subsidence expression on the surface even when they don't persist all the way to surface.

In general, while some faults have naturally served as a limiting boundary for further cave growth, other faults at depth have pulled out the fractured and mobilized zone, effectively increasing its footprint. The predicted crater and fracture limits at the end of mine life have an approximate diameter of 2700 and 3000 m, respectively, as shown in Figure 16. Additionally, the fracture limit lies at a minimum approximate distance of 340 m from the Apache Leap and 1050 m from the Devil's Canyon. Also at the end of mine life, the cave angles are expected to be of the order of 70–78°, with a maximum crater depth of approximately 340 m.

As a conservative approach, the tolerances for bridges can be used to assess the risk of damaging highways. As summarized by Harrison (2011), Moulton et al. (1985) suggest a tolerable magnitude of angular distortion to be between 4×10^{-3} to 5×10^{-3} . As shown in Figure 15, the angular distortion experienced in the vicinity of highway US-60 is less than 1×10^{-3} , suggesting that the caving operation analyzed here is not expected to cause damage to the highway that would impair its serviceability.

The results also suggest that the caving operation would induce no damage to the Devil's Canyon nor the Apache Leap.

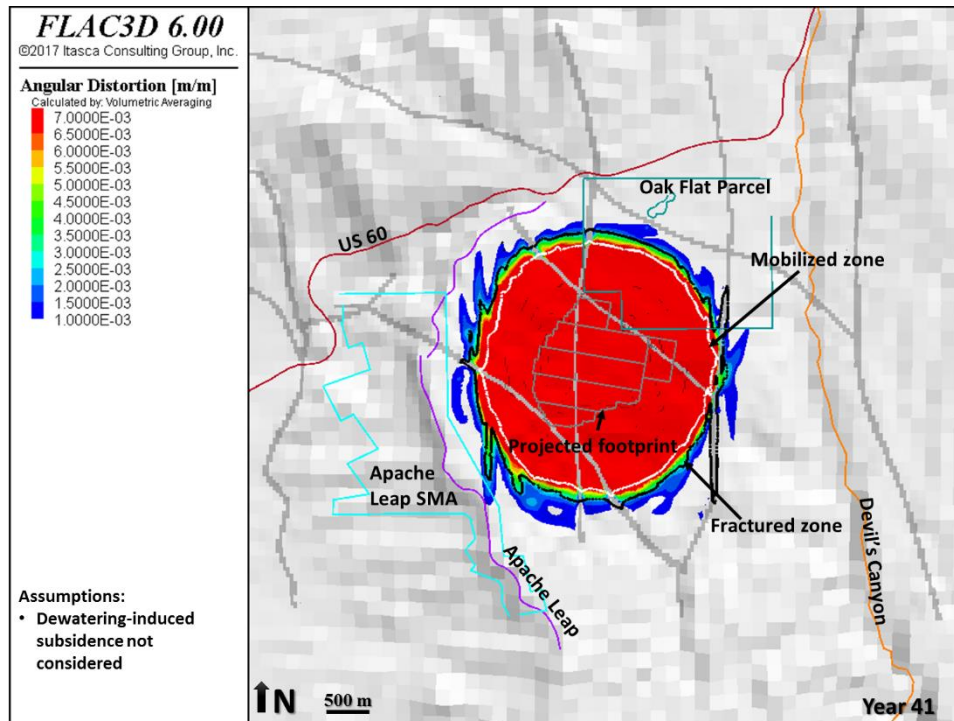


Figure 15 Angular distortion at surface at the end of mine life.

A summary of the evolution over time of the crater (mobilized), fracture, and continuous subsidence limits (as described in Figure 12) are shown in Figure 17. It is important to note that the actual limits predicted by the numerical model are much more irregular (as shown in Figure 16) than suggested by the limits indicated in Figure 17, which were drawn to encompass all regions of persistent shear localizations and produce a conservative smoothed line for ease of visual representation for surface impacts.

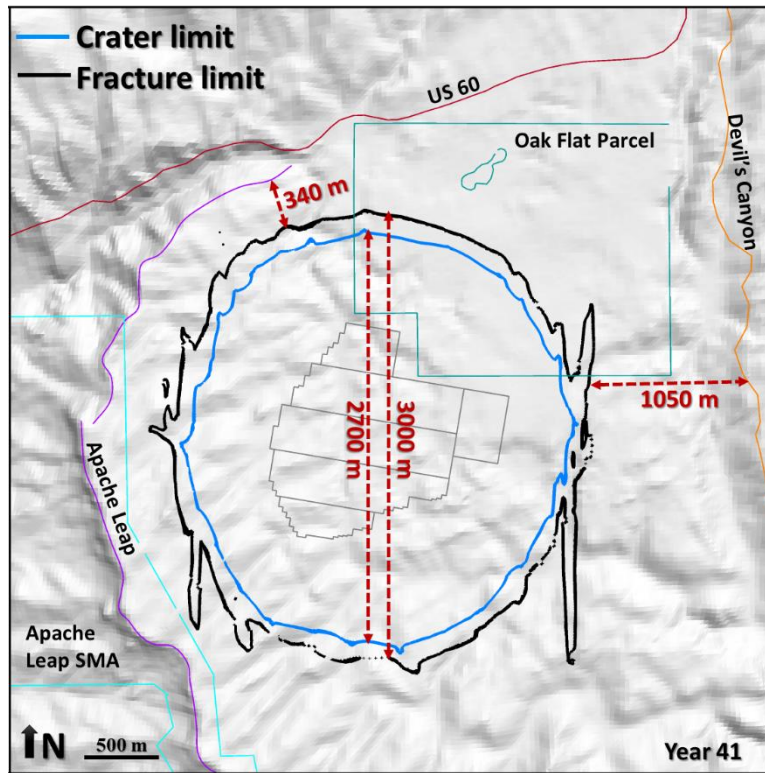
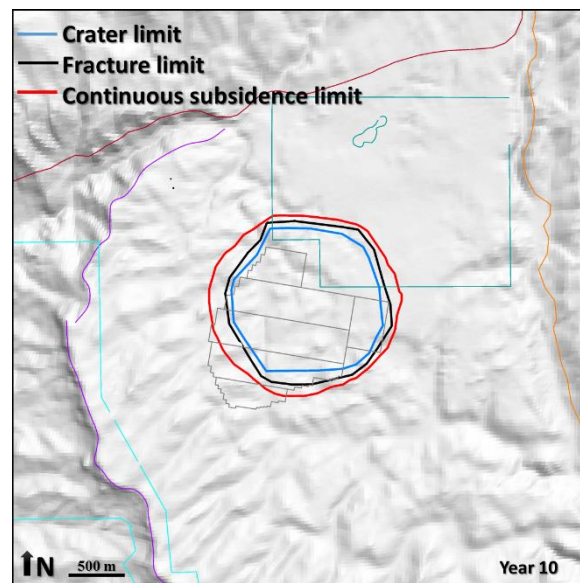
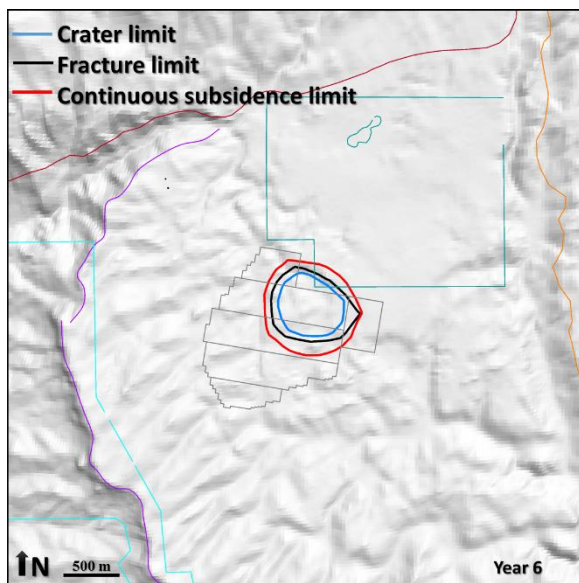


Figure 16 Predicted crater (blue) and fracture limits (black) at the end of mine life.



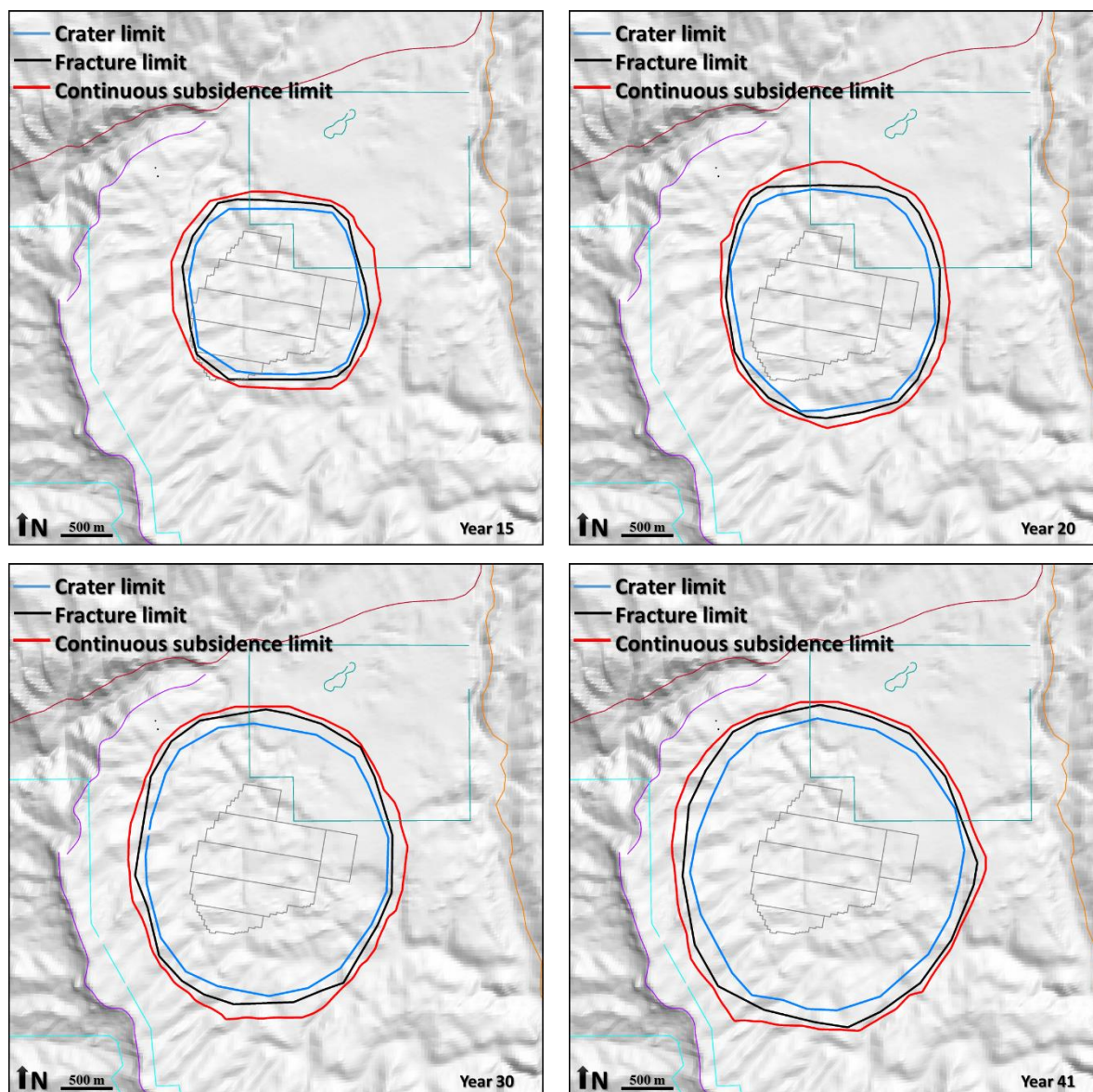


Figure 17 Evolution over time of the crater, fracture and continuous subsidence limits predicted to exist.

In summary, the results of the subsidence impact analysis show the following:

- A caving rate between 5.8 and 16.8 (see Figure 13), with the fracture limit reaching the ground surface around Year 6.
- The average bulking factor of rock within the mobilized zone limits is predicted to increase gradually from 11.4% at year 5 to approximately 15.8% at year 41.
- Cave angles are predicted to be of the order of 70–78°, with a maximum crater depth of approximately 340 m (1115 ft) at the end of mine life.

- While some faults naturally serve as a limiting boundary for further cave growth, other faults at depth would pull out the fractured and mobilized zone, effectively increasing its footprint.
- No damage to the Devil's Canyon nor the Apache Leap, with the fracture limit at a minimum distance of approximately 340 m (1115 ft) from the Apache Leap and 1050 m (3445 ft) from the Devil's Canyon.
- Would not affect the serviceability of highway US-60.

7.0 CONCLUSIONS

The caving simulations conducted for Resolution Copper suggest good caveability, with the cave reaching the ground surface at approximately year 6. This is due to the high ratio of in-situ horizontal stress to rock mass strength ratio. The results suggest a caving rate between 5.8 and 16.8, which compares well with other operations around the world.

The average bulking factor of rock within the mobilized zone limits is predicted to increase gradually from 11.4% at year 5 to approximately 15.8% at year 41. At the end of mine life, the cave angles are expected to be of the order of 70–78° with a maximum crater depth of approximately 340 m (1115 ft). The cave aims to achieve a circular shape in plan, as this is the most stable (due to the confining effects of hoop stress).

The model predicts that caving would not affect the serviceability of highway US-60, and no damage is predicted to the Devil's Canyon nor the Apache Leap. The fracture limit is predicted to stay at a minimum distance of approximately 340 m (1115 ft) from the Apache Leap and 1050 m (3445 ft) from the Devil's Canyon.

While some faults naturally serve as a limiting boundary for further cave growth, thereby compartmentalizing the cave, other faults at depth pull out the fractured and mobilized zone, effectively increasing its footprint

8.0 REFERENCES

Boscardin, M. D. and Cording E. J. (1989) “Building response to excavation-induced settlement,” *Journal of geotechnical engineering* **115**(1). 1-21. ISSN: 0733-9410.

Flores, G. & Karzulovic A. (2002) *Geotechnical Guidelines for a Transition from Open Pit to Underground Mining*. Benchmarking Report for ICSII, Task 4. 392pp.

Fuenzalida, M. and M. Pierce. (2017) “Cave Propagation Analysis at Ghaghoo mine,” Itasca Consulting Group, Inc., Report to Gem Diamonds. Minneapolis, Minnesota.

Fuenzalida, M., T. Katsaga, and M. Pierce. (2017) “Cave Propagation Analysis and Drift Stability Assessment at Henderson Mine 7700SW”, Itasca Consulting Group, Inc., Report Climax Molybdenum Company. Minneapolis, Minnesota.

Itasca Consulting Group, Inc. (2017) *FLAC3D — Fast Lagrangian Analysis of Continua in Three Dimensions* (Version 6.0). Minneapolis: Itasca.

Moulton, L.K., Ganga Rao, H.V.S., and Halvorsen, G.T. (1985) “Tolerable Movement Criteria for Highway Bridges,” Report FHWA/RD-85/107. Washington, DC: Federal Highway Administration.

Sainsbury, B. L. (2010) “Sensitivities in the Numerical Assessment of Cave Propagation,” in *Caving 2010 (Proceedings, Second International Symposium on Block and Sublevel Caving, Perth, Australia, April 2010)*, pp. 523-535. Y. Potvin, Ed. Perth: Australian Centre for Geomechanics.

Sainsbury, D. P., B. L. Sainsbury and L. L. Lorig. (2010) “Investigation of Caving Induced Subsidence at the Abandoned Grace Mine,” in *Caving 2010 (Proceedings, Second International Symposium on Block and Sublevel Caving, Perth, Australia, April 2010)*, pp. 189-204. Y. Potvin, Ed. Perth: Australian Centre for Geomechanics.

Appendix I

1.0 NUMERICAL APPROACH TO ANALYSIS OF CAVING

This section contains a general description of the caving algorithm that applies to all types of caving operations (block cave, panel cave, sublevel cave). It has been used to simulate cave growth successfully at many other mines around the world.

1.1 *FLAC3D*

The caving predictions outlined in this report employ *FLAC3D* (Itasca, 2017), a three-dimensional explicit finite-difference program for engineering mechanics computation. The basis for this program is the well-established numerical formulation used by the two-dimensional program *FLAC*. *FLAC3D* extends the analysis capability of *FLAC* into three dimensions, simulating the behavior of three-dimensional structures built of soil, rock, or other materials that undergo plastic flow when their yield limits are reached. Materials are represented by polyhedral elements within a three-dimensional grid. Each element behaves according to a prescribed linear or nonlinear stress/strain law in response to applied forces or boundary restraints.

The material can yield and flow and the grid can deform (in large-strain mode) and move with the material that is represented. The explicit, Lagrangian calculation scheme and the mixed-discretization zoning technique used in *FLAC3D* ensure that plastic collapse and flow are modeled accurately. Because no matrices are formed, large three-dimensional calculations can be made without excessive memory requirements.

1.2 Conceptual Model of Caving

Five key geomechanical zones are associated with caving, as shown in the conceptual model sketched in Figure 18. This builds on the conceptual model developed by Duplancic and Brady (1999). The following are defining characteristics of each of the five zones.

- **Elastic Zone:** Induced stresses may be high here but are insufficient to induce measurable microseismicity.
- **Seismogenic Zone:** This is where microseismicity occurs within the jointed rock via joint slip and fracture extension. This commonly is defined via an empirical damage threshold criterion that is a function of the deviatoric stress and intact UCS [$0.3 < (\sigma_1 - \sigma_3) / (UCS_{\text{intact}}) < 0.5$].
- **Yielded Zone:** This is where the rock mass has disintegrated and lost all of its cohesive and/or tensile strength but has not moved a significant distance yet. The outer limit of this zone generally coincides with the fracture limit. This is where

visible fractures are evident in intersected openings or on ground surface; significant offset occurs in open boreholes and TDRs break.

- **Air Gap:** An air gap can exist if the overlying rock mass retains some level of cohesive and/or tensile strength. As an air gap expands in size, the overlying rock mass may weaken further, causing the advance of the yielded zone and a collapse into the air gap.
- **Mobilized Zone:** This is where the disintegrated rock mass has moved a significant distance and is starting to dilate and bulk as a result. This criterion depends on the scale of the cave and the modulus of the rock mass, but it is typically represented by 1–2 m of vertical displacement.

The caving algorithm as implemented in *FLAC3D* attempts to predict the limits of these zones as a function of production from the cave. In addition to these cave limits, the results of cave-scale modeling are used to derive estimates of: 1) caveability; 2) abutment and cave stresses; 3) bulking factors, caving rate, and breakthrough timing; and 4) subsidence.

Successful comparisons between predicted (via *FLAC3D*) and actual cave behavior have been achieved at a number of operations worldwide (e.g., Northparkes E26 [Pierce et al., 2006], Palabora [Sainsbury et al., 2008], Grace Mine [Sainsbury et al., 2010], Henderson Mine [Sainsbury et al., 2011], Ghaghoo mine [Fuenzalida et al., 2015a], and Henderson 7700SW [Fuenzalida et al., 2015b]).

The following sections describe the constitutive model and supplemental relations that constitute the algorithm.

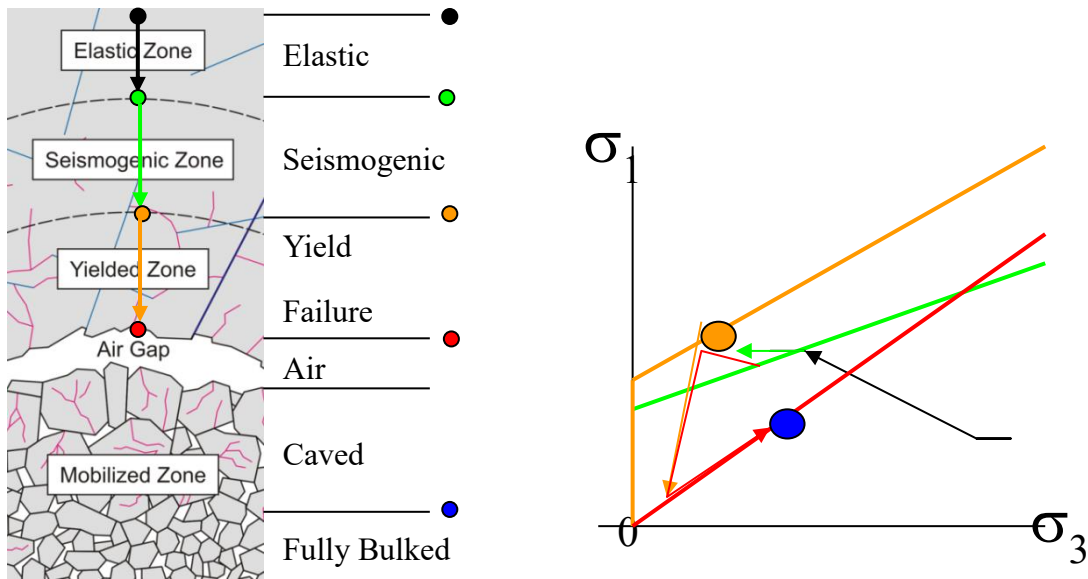


Figure 18 Conceptual model of caving with corresponding stress path through the different stages.

1.3 Background

The numerical approach to cave assessment has been developed over the past 20 years during the industry-funded International Caving Study (ICS I & II) and Mass Mining Technology (MMT) projects. It has been implemented successfully in the simulation of cave responses at a number of operations and projects (Table 5).

Table 5 Applications of Caving Algorithm by Itasca

Operations			Projects	
Andina	Fabian	Koffiefontein	Bingham	Kemess
Argyle	Finsch	New Afton	Cadia East	Niobec
Cullinan	Grace	Northparkes	Chuquicamata	Orapa
Ekati	Henderson	Palabora	Ernest Henry	Oyu Tolgoi
El Salvador	Kapten	Ridgeway Deeps	Far South East	Resolution
El Teniente	Kiruna		Jwaneng	Venetia

The caving and stress-redistribution processes inherently involve large deformations, shear along pre-existing joints and bedding surfaces, fracturing of intact rock blocks, and fragmentation of the rock mass.

An algorithm to simulate caving has been developed within the concept of a continuum-based model. The constitutive rock-mass response required to represent caving (i.e., rock-mass yield, weakening, dilation, and bulking) was developed using strain-softening material models, with strain-dependent properties adjusted to reflect the impacts of dilation and bulking that accompany caving. This algorithm, which has been implemented in Itasca’s three-dimensional numerical code *FLAC3D*, allows the following to be done.

- Development of a large, three-dimensional mine layout and progressive advance of undercutting and draw.
- Production-driven progression of the yielded zone up from the undercut and production areas, and the associated loss of cohesion and tensile strength associated with the rock mass failure.
- Simulation of continuous upward advance of the yielded zone when a sufficient hydraulic radius of the undercut has been achieved (emergent, not imposed within the caving algorithm).
- Stalling of the yield zone and associated air-gap development prior to achieving critical hydraulic radius or when the cave advances through more competent ground.
- Mobilization of yielded ground, and associated dilation and bulking with continued draw.
- Modulus softening as a function of bulking.
- Dilation shut-off at the maximum bulking limit.
- Simulation of cave impact on surface subsidence.

- Redistribution of stress to abutments and pillars resulting from cave propagation.
- Prediction of a seismic and seismogenic zones accompanying the cave propagation.

The algorithm operates on the continuum elements that represent the jointed rock mass, but explicit fracturing representing faults or bedding planes may be added as well. The *FLAC3D* zones (elements) within the cave model typically are quite coarse (approximately 10 m x 10 m x 10 m) to ensure reasonable model run times. Within the caving model, a rigorous mass-balance routine is implemented to ensure that the tonnes-based production schedule is represented accurately within the numerical model. Figure 19 presents a flow chart depicting the caving algorithm.

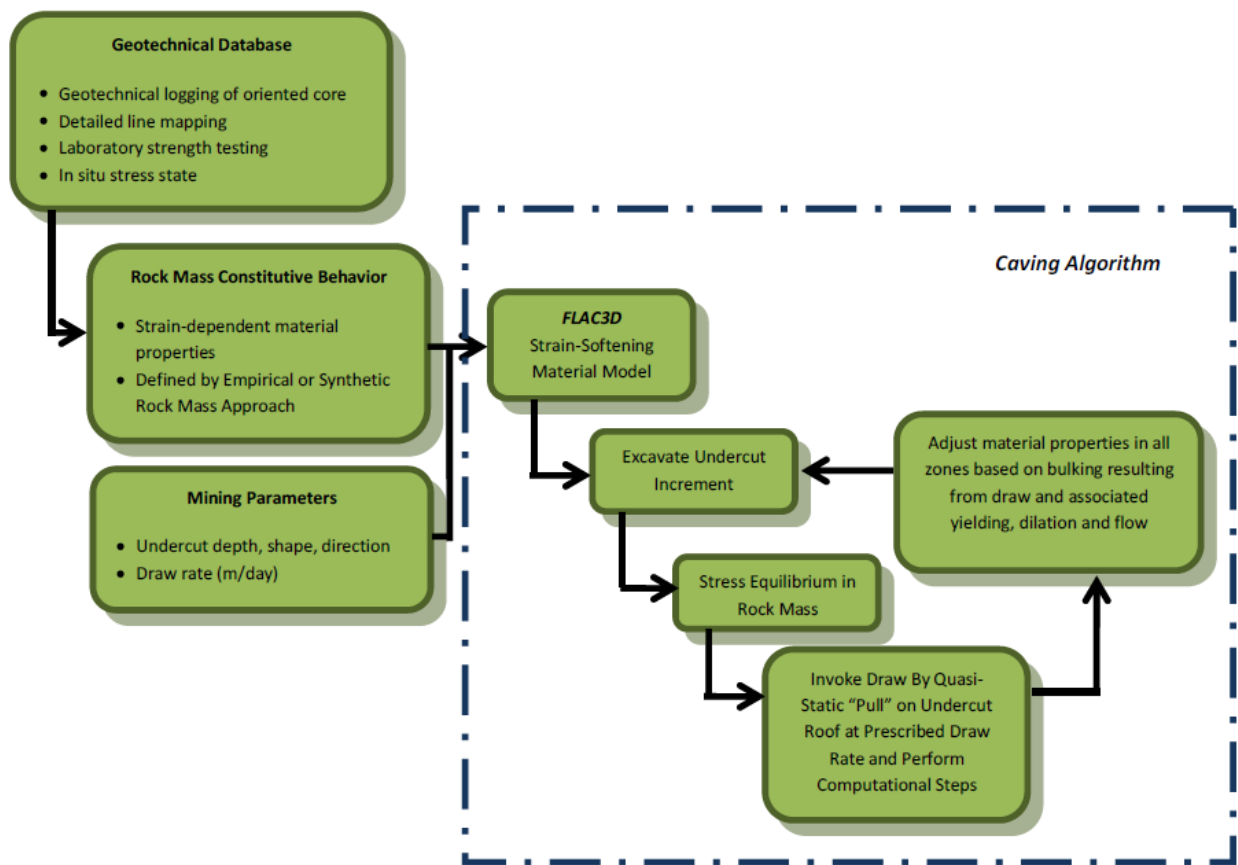


Figure 19 Flow chart for the caving algorithm.

Although the routine is computationally intensive and can lead to relatively long model run-times (two to three weeks), the numerical approach is required to accurately capture the mechanisms of damage, yield, dilation, and bulking necessary to reproduce the evolving cave shape and propagation rates correctly in response to a step-wise production schedule.

FLAC3D offers advanced post-processing of the caving simulation. For example, three-dimensional isosurfaces can be output graphically (Figure 20) to outline the limits of yield and movement, which are defined within the context of the conceptual model for caving. Predictions of seismogenic and aseismic zones can be made using correlations of the onset of microseismicity based on empirical damage criteria. The import of mining layout DXF files is also possible and can be used to plot expected stresses and deformation on the infrastructures.

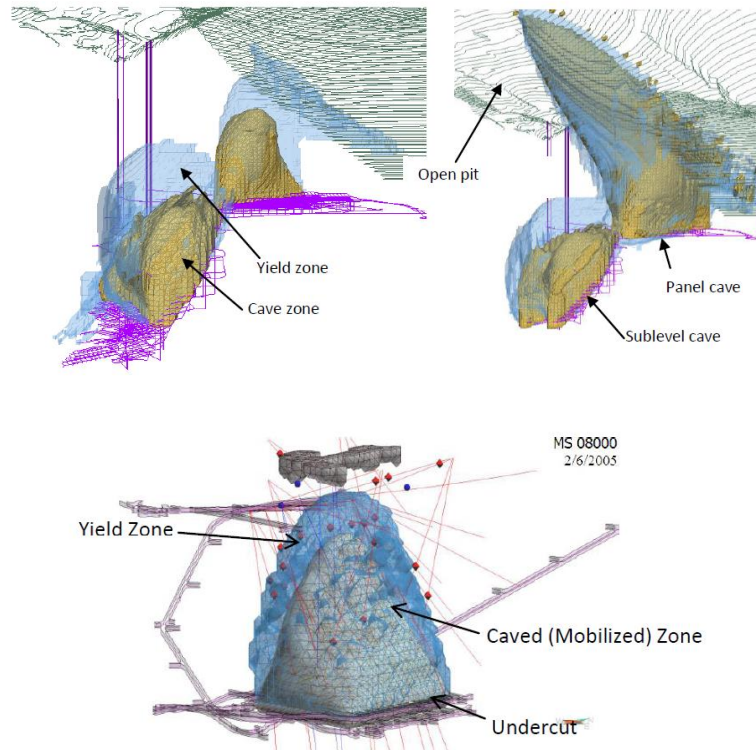


Figure 20 *Isosurfaces of mobilized and yielded zones for two separate panels beneath an overlying open pit (top) and for a block cave at depth (bottom). These predictions are performed using the caving algorithm and FLAC3D.*

1.4 The Cave-Hoek Constitutive Model

A numerical model that represents the caving process must account for the progressive failure and disintegration of the rock mass from an intact/jointed to a caved material. In this complex process, creation of the cave results in: 1) deformation and stress redistribution of the rock mass above the undercut; 2) failure of the rock mass in advance of the cave with associated progressive reduction in strength from peak to residual levels; and 3) dilation, bulking, fragmentation, and mobilization of the caved material. The failure process is characterized by shearing along pre-existing joint surfaces and stress-induced fracturing of intact rock blocks. The failure process will require shear or tensile failure of intact rock bridges between joint segments as the rock mass fragments. This overall process—loading of the rock mass to its peak strength,

followed by a post-peak reduction in strength to some residual level with increasing strain—often is termed a “strain-softening” process and is the result of strain-dependent material properties.

The caving algorithm makes use of the strain-softening Cave-Hoek constitutive model in *FLAC3D*, developed specifically for the caving algorithm, which allows for representation of modulus softening, density adjustment, dilation, dilation shutoff, scaling of properties to zone size, cohesion weakening, tension weakening, and frictional strengthening.

Appendix 1 describes the underlying constitutive model (Cave-Hoek) in more detail.

1.5 Draw Simulation

The drawpoint layout and schedule are defined via external ASCII files. Production marches forward in time increments within the model from the start of the input schedule. To simulate draw, a layer of zones encompassing all active drawpoints for the current year are deleted within the model (Figure 21).

Forces are applied to gridpoints on the floor of the deleted volume to represent the resistance provided by the extraction level, while the gridpoints on the roof of the deleted volume have a small downward velocity applied to them that is proportional to the relative draw rate for the nearest drawpoint. The largest pull velocity (i.e., for the drawpoints with the highest production rate) is set low enough to ensure pseudo-static equilibrium throughout the model (to allow natural gravitational flow of the material and to avoid dynamic “pulling” of the overlying material).

As noted in the previous section, the model is run in small-strain mode (i.e., gridpoint coordinates are not updated) to avoid problems related to extreme deformation of the grid; thus, the density of the zones within the cave must be updated constantly (based on the emergent volumetric strain) to maintain mass balance. The mass of material “drawn” is calculated by monitoring the vertical displacement of zones located directly above the extraction level. Once the vertical displacement of a zone is greater than the distance between this zone and the extraction level, it is considered as having been extracted.

As the mass is drawn from the model, displacement and yielding can occur in the overlying zones (dictated by the stress state and yield strength of the rock mass), and the cave may progress upward. The process is repeated for the remaining years in the schedule. As old drawpoints cease production, the undercut zones are converted to a cohesionless caved-rock material with a modulus consistent with the Pappas and Mark relations for a bulking factor of 25%. This allows stresses to redistribute back into exhausted areas of the cave.

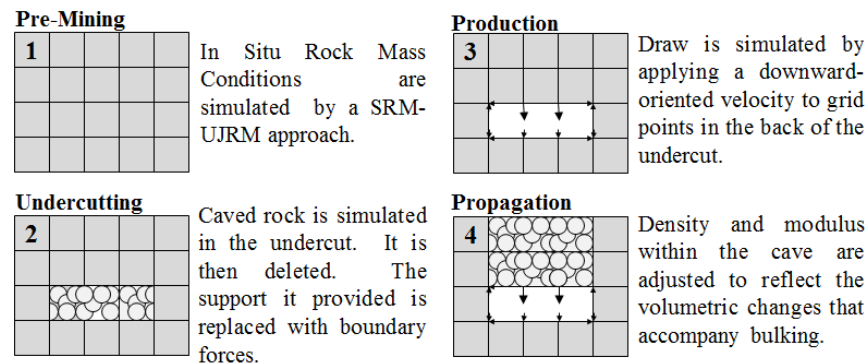


Figure 21 Schematic of the draw simulation.

1.6 Bulked Rock Properties

1.6.1 Maximum Porosity

A literature review conducted by Pierce (2010) suggests that the maximum porosity of angular rockfill is in the range of 0.4 to 0.5, which is equivalent to a bulking factor of 0.66 to 1.0. A maximum porosity in this range is employed in caving simulations. It is important to note that only portions of the cave (typically the boundaries where shearing is maximal) will exhibit the maximum bulking factor and that large volumes of ground in the center of the cave can move down with far less bulking, resulting in an average bulking factor for the cave that is close to what is typically estimated in reality (i.e., 15–20% bulking factor).

1.6.2 Hoek-Brown Residual Properties

Peak strength generally is estimated via GSI and the Hoek-Brown criterion, and sometimes is supplemented with strengths (or other properties) derived from Synthetic Rock Mass (SRM) testing. Residual strength typically is set to that of a bulked rockfill (i.e., zero cohesion and a friction angle of 40–45°). It can also be set to that of a fractured but not bulked rockfill (i.e., zero cohesion and a friction angle of 50–55°) to better model the rock mass behavior of the yielded zone around the cave. In this analysis, the latter approach has been used.

2.0 CAVE-HOEK CONSTITUTIVE MODEL

This section describes the Cave-Hoek constitutive model that was used for this study.

2.1 Input Properties

There are 11 input properties to the Cave-Hoek constitutive model that control rock mass strength and behavior. Those properties are:

- rock mass properties;
- GSI (Geological Strength Index);

- m_i ;
- UCS (Uniaxial Compressive Strength);
- a_{residual} ;
- mb_{residual} ;
- s_{residual} ;
- intact Young's modulus (E_i);
- initial density;
- initial bulking factor or VSI (Volumetric Strain Increment);
- maximum bulking factor or VSI;
- rock fragment aspect ratio;
- ubiquitous joint properties;
- tensile strength;
- cohesion;
- friction angle;
- dilation;
- dip; and
- dip direction.

The GSI, m_i , and UCS parameters control the shape of the Hoek-Brown envelope, which is defined by the following equation (Hoek et al., 2002):

$$\sigma_1 = \sigma_3 + UCS \left(mb \frac{\sigma_3}{UCS} + s \right)^a$$

where

$$m_b = m_i \exp\left(\frac{GSI - 100}{28}\right);$$

$$s = \exp\left(\frac{GSI - 100}{9}\right); \text{ and}$$

$$a = \frac{1}{2} + \frac{1}{6} \left(e^{-GSI/15} - e^{-20/3} \right).$$

a_{residual} , m_{residual} , and s_{residual} are the residual strength parameters to which the rock mass softens after reaching peak strength (see appendix 1.6.2).

The intact Young's modulus is used to calculate the rock mass Young's modulus (E_{rm}), using Hoek and Diederichs' (2006) equation, which governs the rock mass elastic behavior.

$$E_{rm} = E_i \left(0.02 + \frac{1}{1 + e^{((60-GSI)/11)}} \right)$$

The bulking factor or volumetric strain increment (VSI) is defined by:

$$B = \Delta V / V_i = n / (1 - n)$$

where ΔV is the change in volume (positive = expansion), V_i is the initial volume, and n is porosity.

The initial bulking factor usually is set to 0 for an undisturbed and unbulked rock.

Dilation shutoff occurs when the bulking factor reaches a user-defined maximum value to reflect the fact that a rock mass cannot bulk indefinitely.

The rock fragment aspect ratio property is used in the modulus softening calculations.

For the ubiquitous joints, tensile strength, cohesion, and friction angle, control the shape of the Mohr-Coulomb envelope. Dip and dip direction are set equal to the structure or joint to represent true dip and dip direction.

2.2 Bulking

During caving, the rock mass will increase in volume (or bulk) due to dilation under shear, or due to volumetric expansion under tension. Thus, the specification of a dilation angle within the numerical model of caving is important as it controls the rate of bulking during shearing, which is a natural consequence of advance or differential draw. Figure 22 shows non-uniform bulking in the mobilized zone as a consequence of the two bulking mechanisms acting simultaneously within the model.

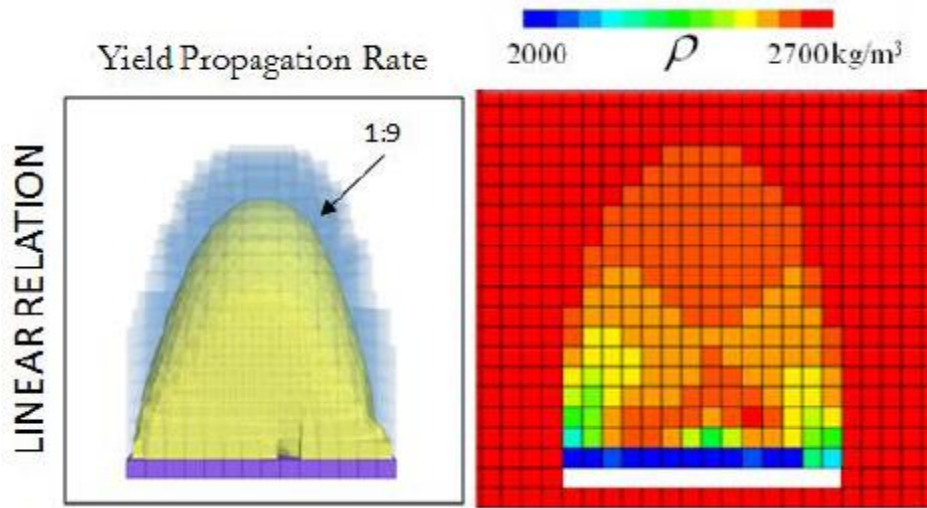


Figure 22 Non-uniform bulking in the mobilized zone (Sainsbury, 2010).

2.3 Density Adjustment

Caving can be simulated in small-strain mode as long as mass balance is maintained. In small-strain mode, node coordinates are not updated and the zone density is adjusted continuously to reflect the volumetric changes that accompany bulking, according to the following relation:

$$\rho_d = \rho_s / (1 + B)$$

$$B = \frac{n}{1 - n}$$

where

- ρ_d = dry density of caved rock;
- ρ_s = solid density of in-situ rock;
- B = bulking factor;
- 1 + B = swell factor; and
- n = porosity.

2.4 Tension Weakening

Tension weakening can occur via two different mechanisms. The growth of new fractures during shear yield is expected to result in tension weakening; thus, the tensile strength of every zone is scaled with cohesion (based on the pre-mining ratio between cohesive and tensile strength). Any

time a zone reaches its peak tensile strength, however, it is presumed to weaken permanently to zero tensile strength in a perfectly brittle fashion (i.e., it is no longer scaled with cohesion).

2.5 Cohesion Weakening

Cohesion weakens linearly with accumulated plastic shear strain (second invariant of the deviatoric plastic strain tensor). The critical shear strain is defined as the total plastic shear strain required to drop the cohesion of a rock mass from peak to zero. At this point, the rock mass is at residual strength (cohesion = 0, tensile strength = 0, and friction = 42°). The smaller the critical plastic strain, the more brittle a rock mass. Figure 23 shows a graphical representation of cohesion weakening.

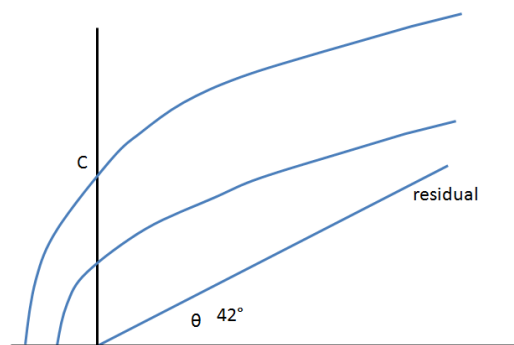


Figure 23 Graphical representation of cohesion weakening.

In the caving model described here, the strain-softening material is described by the Hoek-Brown failure criteria in which mb , s , and a change from peak to residual values as a function of plastic shear-strain.

The critical plastic shear-strain defines the brittleness of the rock mass failure and may be related to the Geological Strength Index (GSI) of the material. This brittleness impacts both the caveability of a given unit, as well as the rate at which a cave will propagate in height for a given amount of draw.

Some generalizations may be made regarding these effects. For example, a higher-quality rock mass (higher GSI) with greater solid rock volume participating in the failure process often will act in a more brittle fashion, thus having a lower critical strain value. Conversely, a lower-quality rock mass (lower GSI) with higher fracture frequency often will act in a more ductile fashion, thus having a larger value of the critical strain.

An estimate of the relation between the critical strain and GSI was determined by a back analysis of rock mass failure in caves and other openings as a part of the MMT project (Lorig, 2000) (Figure 24). The estimate provides a starting point for describing the degree of strain-softening to be used in simulation of caving:

$$\text{critical strain} = (12.5 - 0.125 * \text{GSI}) / (100 * d)$$

where d = zone size.

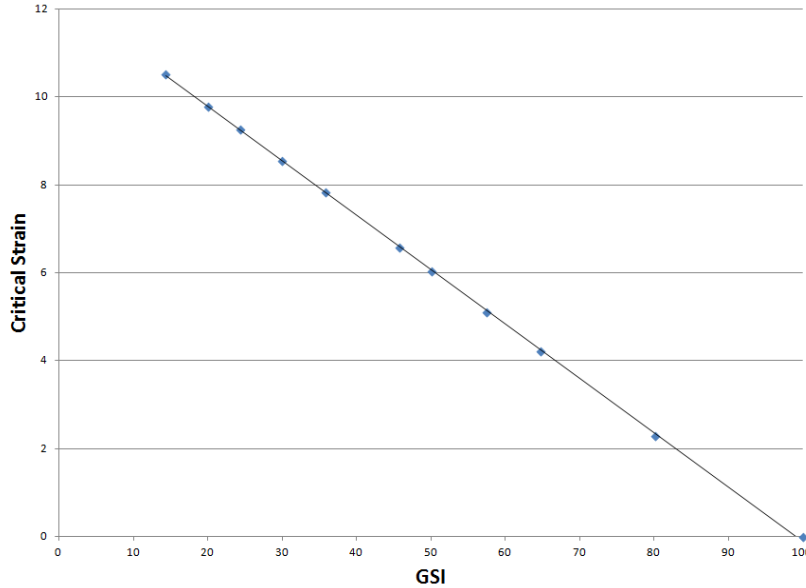


Figure 24 Critical strain vs. GSI relation determined by a back-analysis of rock mass failure in caves and other openings for 1-m zones.

The presence of zone size within this relation recognizes that the critical strain parameter is zone-size dependent in continuum models where shearing tends to be resolved in a band approximately one zone thick.

2.6 Modulus Softening

As a rock mass bulks via shear or tension, it is expected to experience a drop in modulus. Representation of this drop is required in order to account for stress shedding away from the mobilized zone and into the surrounding rock mass. In addition, it is necessary to allow for modulus hardening that can occur when stresses are shed back onto exhausted or undrawn parts of the cave.

The results of laboratory testing by Pappas and Mark (1993) (Figure 25) show that the modulus of rock drops in a non-linear fashion with increased bulking, and that the rate of modulus change is a function of fragment shape and intact strength. Based on the results of these tests, they developed a series of equations that can be used to estimate modulus as a function of bulking factor (BF), uniaxial compressive strength (UCS, in psi) of the intact rock fragments and the aspect ratio of the fragments (Table 6). Note that the Pappas and Mark definition of bulking factor (BF) is different from what typically is used in caving: $BF = 1 + \text{caved-rock bulking factor}$

(defined in this report as B). The chart shown in Figure 26 can be used to estimate the thickness-to-width (aspect) ratio.

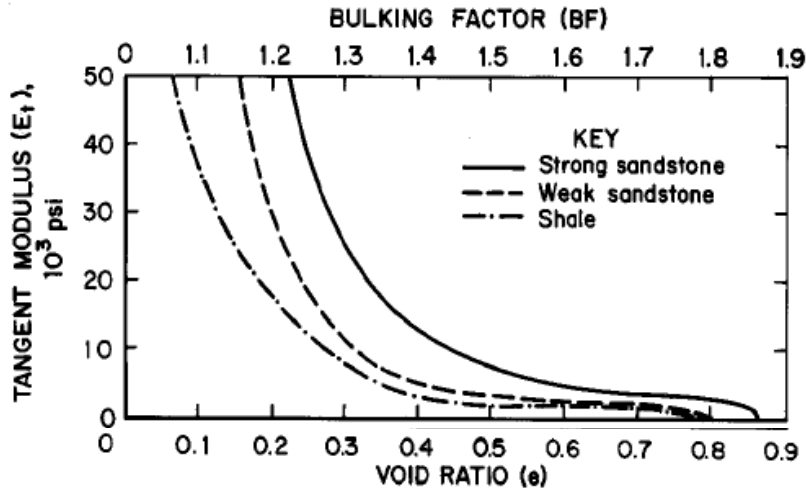


Figure 25 Best-fit tangent modulus (in psi) versus void ratio for all rock types tested by Pappas and Mark (1993). The y-axis (modulus) limit of 50,000 psi in this plot is equal to 345 MPa. The lower x-axis (void ratio) limit of 0.9 is equivalent to a porosity of 47%.

Table 6 Modulus-Softening Equations Developed by Pappas and Mark (1993)

Tangent (E_t) Modulus at Various Bulking Factors (BF) (Pappas and Mark, 1993)	
BF = 1.25	$E_t = 2.49X_1 + 41,200X_2 - 24,800$
BF = 1.30	$E_t = 1.76X_1 + 23,800X_2 - 15,700$
BF = 1.35	$E_t = 1.32X_1 + 16,300X_2 - 11,400$
BF = 1.40	$E_t = 0.933X_1 + 11,300X_2 - 7,900$
BF = 1.50	$E_t = 0.568X_1 + 6,900X_2 - 500$

Note: This is based on laboratory oedometer tests on materials of varying bulking factor (BF), intact strength and fragment shape. X_1 is the uniaxial compressive strength (UCS) of the intact rock fragments (in psi); X_2 is the thickness-to-width (aspect) ratio of the fragments.

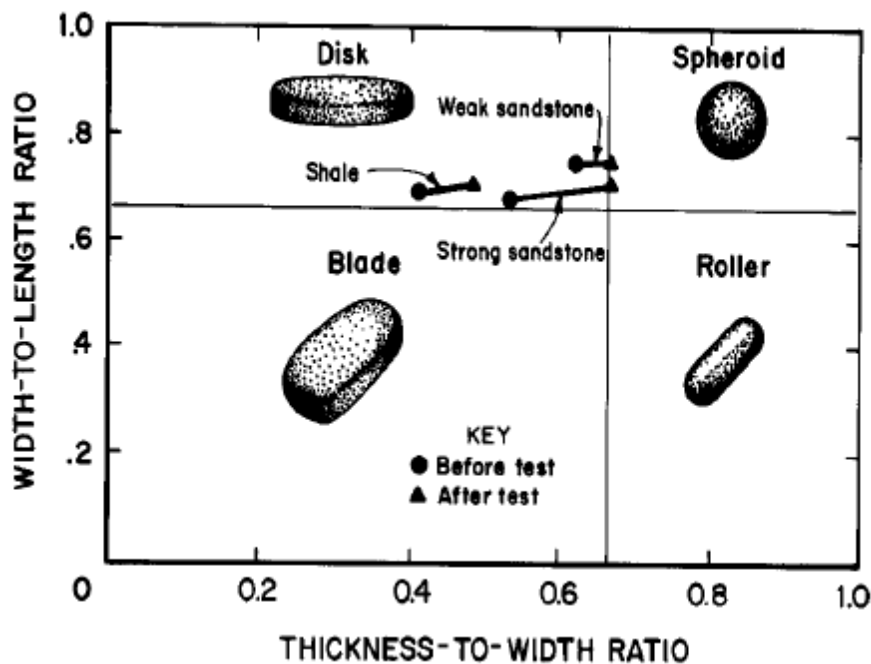


Figure 26 Pappas and Mark (1993) chart for estimation of fragment thickness-to-width ratio.

During production simulation, the caved-rock bulking factor in each zone is given by its volumetric strain. If the caved-rock bulking factor is greater than 0.25, the Pappas and Mark equation is used to establish a new tangent modulus for the zone based on the user-defined UCS, shape factor, and BF (caved rock bulking factor + 1). Each zone within the caving model can have a different UCS and shape factor associated with it. For caved-rock bulking factors less than 0.25, the tangent modulus is calculated through interpolation between the in-situ rock mass

modulus and the Pappas and Mark modulus corresponding to a caved rock bulking factor of 0.25. Figure 27 through Figure 29 show the relations in graphical form as a function of initial modulus, UCS, and shape factor. Because the modulus is updated constantly via the zone-based volumetric strains, it allows for both modulus softening (during bulking) and modulus hardening (e.g., during recompaction of exhausted or undrawn parts of the cave).

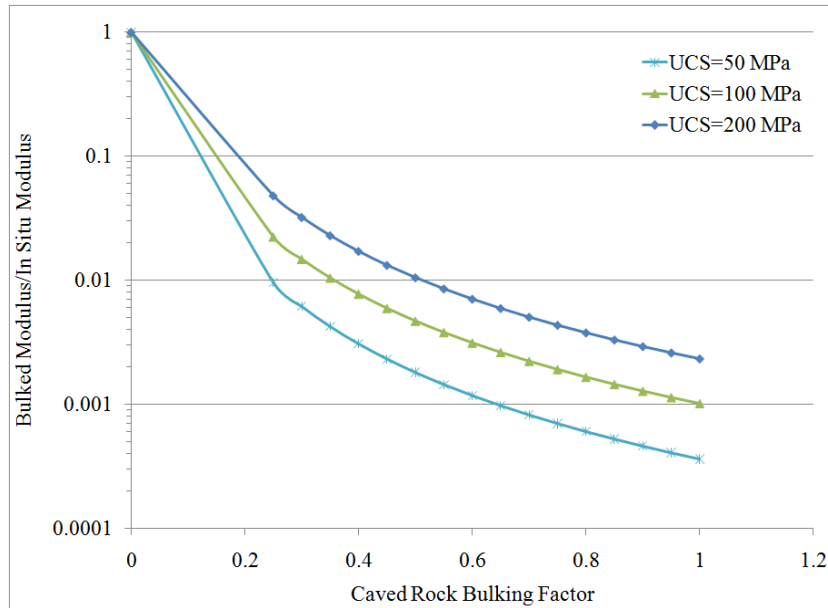


Figure 27 Sensitivity of Pappas and Mark modulus-softening relations, to UCS ($E_i = 10$ GPa, aspect ratio = 0.5).

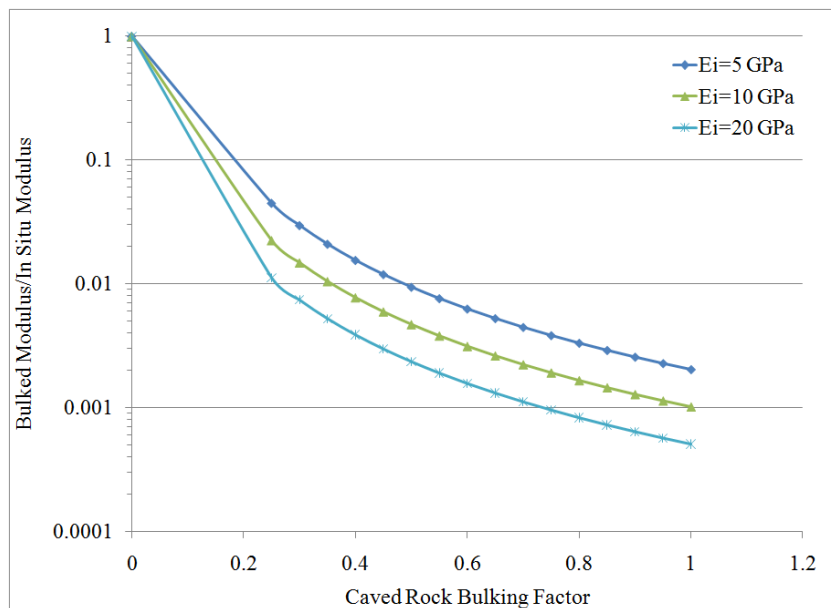


Figure 28 Sensitivity of Pappas and Mark modulus-softening relations, initial rock-mass modulus, E_i (UCS = 100 MPa, aspect ratio = 0.5).

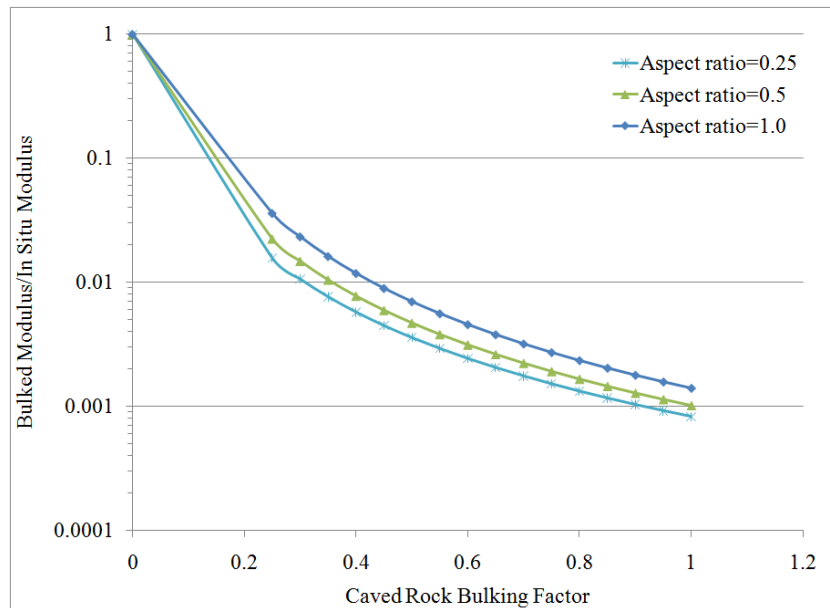


Figure 29 Sensitivity of Pappas and Mark modulus-softening relations, fragment aspect ratio ($UCS = 100\text{ MPa}$, $E_i = 10\text{ GPa}$).

2.7 Dilation Shutoff

Within the existing numerical model of caving, dilation angle is set as a standard material property, but is set to zero when a user-defined maximum bulking factor is reached. This latter behavior is built into the Cave-Hoek constitutive model and prevents zones from expanding to unrealistic levels during shear. The dilation angle of the rock mass is assumed to be equal everywhere to 10° based on guidelines provided by Hoek and Brown (1997). Figure 30 presents a graphical representation of dilation shutoff.

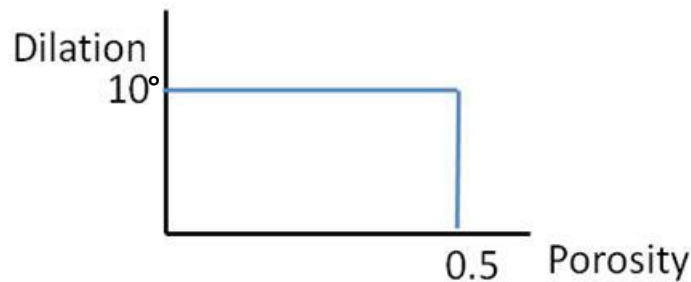


Figure 30 Graphical representation of dilation shutoff.